



X-Ray and Ultraviolet Flares on AT Microscopii Observed by AstroSat

A. A. Kuznetsov^{1,2} , R. R. Karakotov¹, K. Chandrashekhar^{3,4} , and D. Banerjee^{5,6,7}

¹ Institute of Solar-Terrestrial Physics, Irkutsk, 664033, Russia; a_kuzn@iszf.irk.ru

² Department of Geography, Irkutsk State University, Irkutsk, 664033, Russia

³ Rosseland Centre for Solar Physics, University of Oslo, PO Box 1029, Blindern 0315 Oslo, Norway

⁴ Institute of Theoretical Astrophysics, University of Oslo, PO Box 1029, Blindern 0315 Oslo, Norway

⁵ Aryabhata Research Institute of Observational Sciences (ARIES), Manora Peak, Nainital 263002, India

⁶ Indian Institute of Astrophysics, Sarjapur Main Road, 2nd Block, Bangalore, Karnataka 560034, India

⁷ Center of Excellence in Space Science, IISER Kolkata, Kolkata 741246, India

Received 2022 August 2; revised 2022 November 3; accepted 2022 November 7; published 2022 December 9

Abstract

We present observations of the active M-dwarf binary AT Mic (dM4.5e+dM4.5e) obtained with the orbital observatory AstroSat. During 20 ks of observations, in the far-ultraviolet (130–180 nm) and soft X-ray (0.3–7 keV) spectral ranges, we detected both quiescent emission and at least five flares on different components of the binary. The X-ray flares were typically longer than and delayed (by 5–6 minutes) with respect to their ultraviolet counterparts, in agreement with the Neupert effect. Using X-ray spectral fits, we estimated the parameters of the emitting plasma. The results indicate the presence of a hot multi-thermal corona with average temperatures in the range of $\sim 7\text{--}15$ MK and emission measure of $\sim (2.9\text{--}4.5) \times 10^{52} \text{ cm}^{-3}$; both the temperature and the emission measure increased during the flares. The estimated abundance of heavy elements in the corona of AT Mic is considerably lower than at the Sun ($\sim 0.18\text{--}0.34$ of the solar photospheric value); the coronal abundance increased during the flares due to chromospheric evaporation. The detected flares had the energies of $\sim 10^{31}\text{--}10^{32}$ erg; the energy-duration relations indicate the presence of magnetic fields stronger than in typical solar flares.

Key words: stars: coronae – stars: flare – stars: late-type – X-rays: stars – ultraviolet: stars

1. Introduction

Many dwarf stars, including the Sun, demonstrate signatures of magnetic activity, such as starspots, hot coronae and flares (Gershberg 2005). Cool red dwarfs of dMe spectral type are usually much more active than the Sun, which is manifested in stronger magnetic fields, hotter and denser coronae with a persistent presence of nonthermal electrons, and more frequent and powerful flares (Haisch et al. 1991; Güdel 2002, 2004; Reiners 2012); nevertheless, the physical mechanisms responsible for the coronal heating and flares are believed to be qualitatively similar to the solar ones.

Observations in the soft X-ray range provide an opportunity to study thermal plasma in stellar coronae and determine its parameters, such as density, temperature, emission measure (EM) and chemical composition—both in the quiescent state and during flares (Güdel 2004). On the other hand, optical and ultraviolet (UV) emissions of flares are produced in deeper layers of stellar atmospheres (the chromosphere and transition region), in response to heating of these layers by nonthermal electron beams (Benz & Güdel 2010); the optical continuum is responsible for most part of the radiated flare energy (Kretzschmar 2011). Simultaneous observations in different spectral ranges (e.g., soft X-rays and UV) are of special interest, because they allow one to study the processes at different layers of a stellar atmosphere and,

in particular, investigate correlations between thermal and nonthermal processes. While the Sun is continuously observed by many instruments providing a broad spectral coverage (from radio to γ -rays), multiwavelength observations of flares on other stars are much less common. Thus expanding the data set of such observations (both for the same or for different targets) is highly important, because it improves the reliability of the derived physical models, as well as allows one to study long-term variations of stellar active phenomena, including activity cycles.

In this work, we investigate the well-known active M-dwarf binary AT Microscopii (AT Mic) using observations with the orbital observatory AstroSat; manifestations of stellar activity were detected in X-ray and UV spectral ranges. We analyze the characteristics of the coronal plasma in the quiescent and flaring states; we also investigate the relationship between the X-ray and UV flares. We compare the obtained results with earlier observations of AT Mic and other red dwarfs, as well as with observations and models of solar flares.

2. Observations

2.1. Target

AT Mic is a visual binary consisting of two almost identical red dwarfs of spectral type dM4.5e (Joy & Abt 1974), at a distance of 9.86 pc (Gaia Collaboration 2020). The binary is

sufficiently wide, with a semimajor axis of ~ 31 au and an orbital period of about 209 yr (Malkov et al. 2012), so that interaction between the components is negligible, i.e., in terms of magnetic activity, they can be considered as two separate single stars. AT Mic is believed to be a member of the β Pictoris association, with an age of ~ 25 Myr (Messina et al. 2017). The rotation periods of components A and B are 1.19 and 0.78 days, respectively (Messina et al. 2016, 2017); the bolometric luminosities of components A and B have been estimated as 1.3×10^{32} and 1.2×10^{32} erg s $^{-1}$ (0.034 and 0.031 L_{\odot}), respectively (Messina et al. 2017). Both components are known to be magnetically active (e.g., Gershberg et al. 1999).

Due to its proximity and high activity level, AT Mic has been a target of many observations in different spectral ranges. Powerful optical flares with energies of up to $\sim 4 \times 10^{33}$ erg were reported by Kunkel (1970), Nelson et al. (1986), García-Alvarez et al. (2002), etc. Pallavicini et al. (1990), Raassen et al. (2003), Robrade & Schmitt (2005), etc., observed AT Mic in the soft X-ray range and detected quiescent emission of hot coronal plasma with a luminosity of $\sim 2 \times 10^{29}$ erg s $^{-1}$, as well as a number of flares with energies of up to $\sim 1.3 \times 10^{33}$ erg. Linsky et al. (1982), Elgaroy et al. (1988), Monsignori et al. (1995), etc., detected quiescent chromospheric emission and flares in the UV range, while Mitra-Kraev et al. (2005) investigated correlations between X-ray and UV flares. The durations of the detected flares varied from less than one minute up to about one hour, with the above mentioned energies corresponding to the longest and most powerful flares.

2.2. Observations with AstroSat

We observed AT Mic with the instruments onboard the AstroSat satellite (Singh et al. 2014; Agrawal 2017), on 2018 October 3–4. The primary instrument was the Soft X-ray Telescope (SXT)—an X-ray telescope with focusing mirrors that provides X-ray imaging and spectroscopy in the nominal energy range of 0.3–8 keV with the energy channel width of 0.01 keV (Singh et al. 2016, 2017). The SXT operated in photon counting mode; the total exposure time was 20 ks. A half of that time was also covered by high-resolution imaging observations with the Ultra-Violet Imaging Telescope (UVIT) (Tandon et al. 2017a, 2017b) in the far-ultraviolet (FUV) channel (130–180 nm), in photon counting mode; the F148W filter with the 125–175 nm bandpass was used. The target was detected by both of these instruments, thus providing simultaneous observations in the two spectral ranges for ~ 10 ks.

Simultaneously, AT Mic was observed with two other X-ray detectors: the Large Area X-ray Proportional Counter (LAXPC) (Yadav et al. 2016; Agrawal et al. 2017) in the 3–100 keV energy range, and the Cadmium Zinc Telluride Imager (CZTI) (Bhalerao et al. 2017) in the 25–150 keV energy range. However, no reliable signal of stellar origin was detected

by these instruments, due to either insufficient sensitivity (for the CZTI, given that the X-ray flux decreases rapidly with energy) or a high and rapidly varying instrumental background (for the LAXPC); we do not analyze these observations here.

Multiwavelength observations (including the soft X-ray and UV spectral ranges) of AT Mic and other active red dwarfs were performed earlier with the XMM-Newton observatory (e.g., Mitra-Kraev et al. 2005; Tsang et al. 2012; Perdelwitz et al. 2018). In comparison with the XMM-Newton European Photon Imaging Camera (EPIC) (Strüder et al. 2001; Turner et al. 2001), the AstroSat SXT has a lower sensitivity to soft X-rays, which requires longer accumulation times or time bins to obtain a reliable signal from the same source. On the other hand, in comparison with the XMM-Newton Optical Monitor (OM) (Mason et al. 2001), the AstroSat UVIT has considerably better sensitivity and angular resolution in the far-UV range, which allows one to study the morphology and light curves of UV sources with much finer details.

3. Results

3.1. Images

Figure 1 demonstrates the images of AT Mic obtained with the AstroSat UVIT FUV and SXT, integrated over the entire duration of the observations. Figure 1(a) displays a fragment of the UVIT field of view; the binary components are partially resolved with component A (the northern one) being slightly brighter. Figure 1(b) shows the full SXT field of view (photons in the energy range of 0.3–7 keV were selected, because at higher energies the signal might be contaminated by instrumental noise); the bright spots at the corners of the detector matrix are the internal calibration sources. The X-ray photons are scattered over a relatively wide area, so that the binary components are not resolved; nevertheless, the X-ray centroid position coincides with the AT Mic position with an accuracy of $\sim 1''.5$, and there are no other candidate X-ray sources in this region of the sky.

The circles in Figure 1 indicate the regions used to extract the UV and X-ray light curves and X-ray spectra. For the UV emission, we mainly consider the total flux from both components of the binary, within a radius of $4''.2$. Since the components are resolved only partially, we cannot separate the fluxes from them completely; the partial fluxes from the individual binary components (from the regions shown by white dashed circles with a diameter of $1''.5$, corresponding to the overall FWHM of the UVIT FUV) are analyzed only qualitatively—to identify the component where a flare occurred. For the total X-ray flux, we use the extraction region with a radius of $16'$, which contains more than 96.5% of the source photons (according to the point-spread function presented in the AstroSat Handbook⁸).

⁸ http://www.iucaa.in/astrosat/AstroSat_handbook.pdf

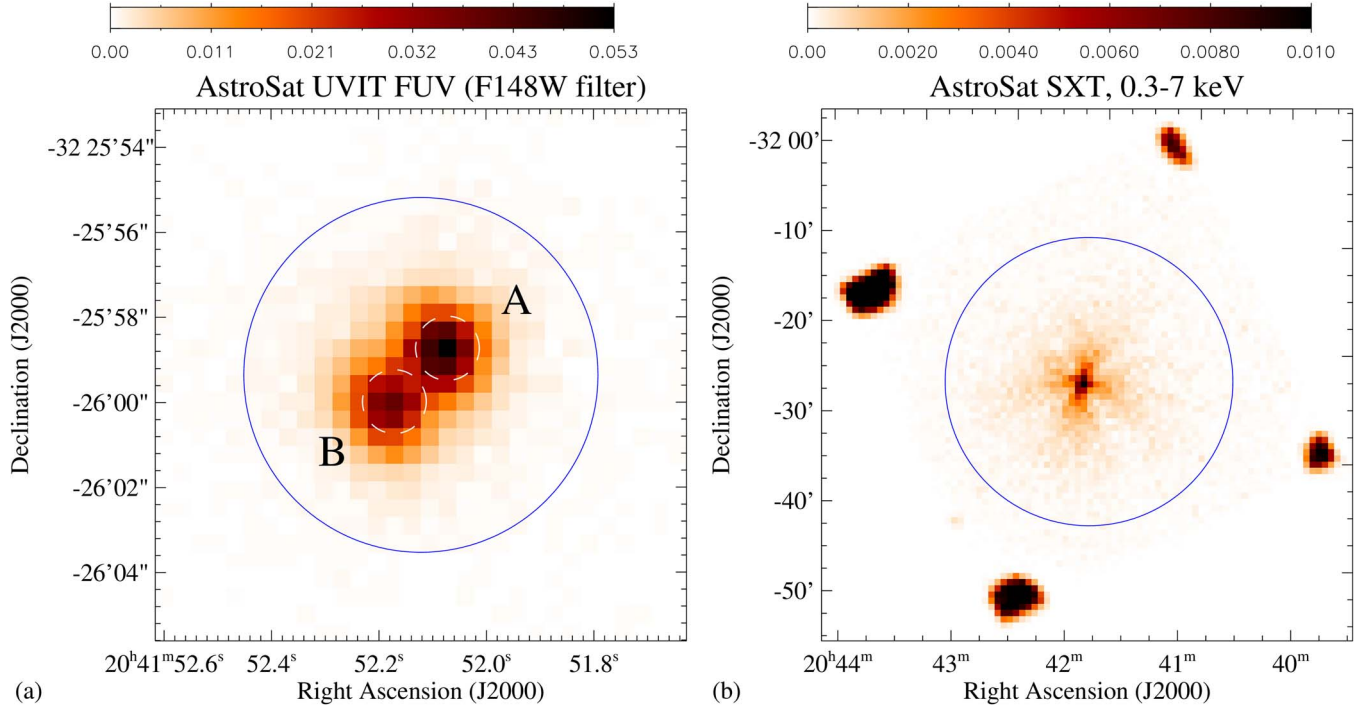


Figure 1. UV (a) and X-ray (b) images of AT Mic from the AstroSat UVIT FUV and SXT observations on 2018 October 3–4, for the entire observation intervals. The color bars are in units of counts s^{-1} pixel $^{-1}$. The blue or white circles indicate the extraction regions for light curves and spectra.

3.2. Light Curves

3.2.1. Light Curves: Overview

Figure 2 demonstrates the total (i.e., combining the fluxes from both components of the binary) X-ray and UV light curves of AT Mic, with the time bin size of 300 s. Due to periodic occultations of the target by the Earth, the light curves are not continuous but consist of a number of shorter time intervals (orbits); due to stricter visibility constraints, the UVIT FUV observing intervals are shorter than those for the SXT, and the UVIT observations ceased after the first eight orbits. For the X-ray light curve, photons in the energy range of 0.3–7 keV were selected and the instrumental background provided by the SXT team⁹ was subtracted; for the UV observations, the instrumental background is negligible.

Identifying the flaring and non-flaring (quiescent) time intervals in our observations is not straightforward, because of the above mentioned gaps in the light curves, and also because of a high activity level: AT Mic spends $\sim 25\%$ of the time in a flaring state, according to Messina et al. (2016), or even more than 50% of time, according to Kunkel (1970). We determined the quiescent background levels by iteratively fitting the light curves with linear functions and removing the data points that exceeded these fits by more than 1σ ; this

procedure effectively provides a linear fit to the lower envelope of a light curve. The X-ray quiescent background tends to increase with time—probably, reflecting the stellar rotation and/or evolution of active regions; the UV quiescent background also demonstrates a weak increase with time.

We consider the time intervals where the UV and/or X-ray fluxes exceeded the respective quiescent background levels by more than 3σ as candidate flares. We have identified five such flaring events scattered over four AstroSat orbits (namely, orbits #16300, #16302, #16306 and #16307; see the next section for details). In addition, we have selected, in the X-ray light curve, two time intervals with the lowest flux (namely, orbits #16303 and #16308), which we consider as a “quiescent state,” although these intervals could still contain weaker unresolved flares.

3.2.2. Light Curves of Flares

We plot in Figure 3 enlarged fragments of the light curves for the time intervals containing flares. Together with the total (unresolved) X-ray and UV light curves of AT Mic, we depict the UV light curves corresponding to the individual components of the binary. The time bins are reduced (in comparison to Figure 2) to 180 s for the X-rays and 100 s for the UV emission. The basic characteristics of the detected flares are summarized in Table 1. In particular, the e -folding decay times of flares τ_X and τ_{UV} (which we use to characterize the flare

⁹ https://www.tifr.res.in/~astro_sat_sxt/dataanalysis.html

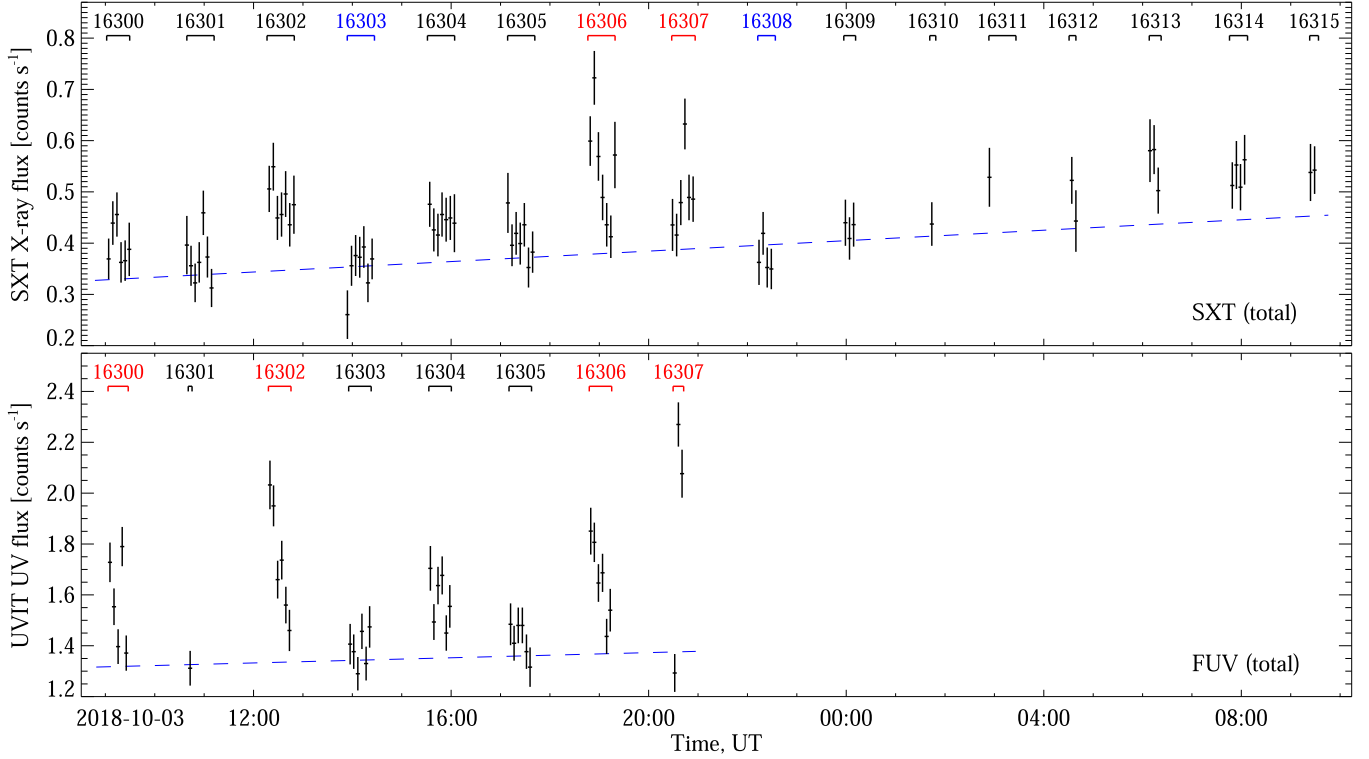


Figure 2. X-ray (top) and UV (bottom) light curves of AT Mic from the AstroSat SXT and UVIT FUV observations on 2018 October 3–4, with 300 s time bins. The error bars correspond to the 1σ level. The blue dashed lines represent the estimated quiescent (non-flaring) background fluxes. The AstroSat orbit numbers are expressed at the tops of the panels, with the supposed flaring or (for X-rays) quiescent-only time intervals indicated by red or blue colors, respectively.

Table 1

Parameters of the Flares Detected on AT Mic: Sources (i.e., Components of the Binary where the Flares Occurred), Decay Times in the X-ray (τ_X) and UV (τ_{UV}) Ranges, Delays of the X-ray Flares with Respect to the Corresponding UV Flares (Δt_{X-UV}), Peak Luminosities in the X-Ray Range (L_X^{\max}) and in the Optical Continuum (L_{cont}^{\max}), Emitted Energies in the X-Ray Range (E_X) and in the Optical Continuum (E_{cont}), and Estimated (Following the Scaling Laws by Namekata et al. 2017) Sizes of the Flaring Regions (L) and Magnetic field Strengths in these Regions (B)

Flare	Source	τ_X min	τ_{UV} min	Δt_{X-UV} min	L_X^{\max} $10^{29} \text{ erg s}^{-1}$	L_{cont}^{\max} $10^{29} \text{ erg s}^{-1}$	E_X 10^{31} erg	E_{cont} 10^{31} erg	L 10^9 cm	B G
F1	B	7.88 ± 7.57	3.67 ± 1.44	4.87 ± 1.72	$0.46^{+0.21}_{-0.19}$	$0.92^{+1.19}_{-0.62}$	$2.19^{+0.77}_{-0.68}$	$3.03^{+3.50}_{-1.94}$	$4.46^{+1.48}_{-1.48}$	$101.1^{+58.0}_{-33.6}$
F2	B	...	2.78 ± 1.15	5.21 ± 1.72	...	$1.19^{+1.43}_{-0.77}$...	$2.20^{+2.56}_{-1.41}$	$3.75^{+1.27}_{-1.28}$	$112.0^{+67.7}_{-37.9}$
F3	B	7.45 ± 5.90	6.54 ± 2.68	0.57 ± 1.72	$0.64^{+0.23}_{-0.21}$	$1.35^{+1.58}_{-0.87}$	$4.14^{+0.99}_{-0.93}$	$6.71^{+6.89}_{-4.10}$	$6.59^{+2.12}_{-2.17}$	$83.8^{+48.7}_{-27.4}$
F4	A, B	10.62 ± 3.97	...	$\gtrsim (5.61 \pm 1.72)$	$1.05^{+0.31}_{-0.26}$	$1.27^{+1.60}_{-0.84}$	$8.71^{+1.68}_{-1.40}$	$> 5.27^{+5.64}_{-3.27}$
F5	A	9.31 ± 7.00	4.30 ± 0.85	5.07 ± 1.72	$0.73^{+0.26}_{-0.22}$	$2.69^{+2.81}_{-1.65}$	$3.77^{+1.05}_{-0.88}$	$\gtrsim 6.81^{+6.82}_{-4.12}$	$\gtrsim 5.59^{+1.31}_{-1.34}$	$\gtrsim 108.0^{+33.6}_{-27.5}$

Note. The peak luminosities (L_X^{\max} and L_{cont}^{\max}) and emitted energies (E_X and E_{cont}) of the flares were estimated using Equations (7)–(11), as described in Section 4.3.1.

durations) are estimated by least-squares fitting the flare decay phases in the total light curves displayed in Figure 3 with exponential functions in the form

$$I(t) = I_{\text{bg}}(t) + A \exp\left(-\frac{t - t_{\text{peak}}}{\tau}\right), \quad t \geq t_{\text{peak}}, \quad (1)$$

where $I(t)$ is the flux in the considered spectral band, $I_{\text{bg}}(t)$ is the estimated quiescent background flux and t_{peak} is the flare peak time. The delays between the X-ray and UV flares

Δt_{X-UV} are defined as delays between the respective flare peaks; the uncertainty in estimating the delays σ_{X-UV} is estimated as $\sigma_{X-UV}^2 = (\Delta t_X/2)^2 + (\Delta t_{UV}/2)^2$, where Δt_X and Δt_{UV} are the time bins of the X-ray and UV light curves, respectively.

In the total UV light curve in Figure 3(a), one can see two well-defined flares, peaked at around 09:07 and 09:19 UT, both with “classical” flare profiles consisting of a sharp rise and a slower exponential decay. Comparison with the light curves of

the individual binary components indicates that both flares occurred on component B. The flares are relatively short—with durations of just a few minutes. In the X-ray light curve, one can see a flare (again, with a “classical” profile) peaked at around 09:12 UT, which likely corresponds to the UV flare F1; however, the X-ray flare is longer than (with the characteristic decay time $\tau_X \simeq 2\tau_{UV}$) and delayed by ~ 5 minutes with respect to its UV counterpart. Later, at around 09:24 UT, there is a barely noticeable X-ray peak—possibly, a counterpart of the UV flare F2. We cannot determine reliably the decay time of this supposed X-ray flare; however, like in the previous event, the X-ray peak is delayed with respect to the UV flare peak by ~ 5 minutes.

In the total light curves in Figure 3(b), one can see a flare (F3) that peaked at around 12:24 UT, nearly simultaneously in the X-ray and UV ranges; the UV flare occurred on component B. In contrast to the previous two flares, the UV flare F3 has a more complicated profile—likely, a result of overlapping of several partially resolved flaring events. The X-ray flare F3 has a nearly triangular shape with comparable rise and decay times. The delay between the X-ray and UV peaks is almost absent, and the flare durations in both spectral ranges are similar ($\tau_X \simeq \tau_{UV}$).

The time interval shown in Figure 3(c) contains the largest and longest X-ray flare (F4) among the detected ones, with a “classical” flare profile, peaked at around 18:54 UT. Interpretation of the UV light curves is less straightforward: at the beginning of the time interval, one can see a UV peak—likely, a tail of a powerful flare that occurred on component A; if this UV flare indeed corresponds to the X-ray flare F4, the delay between the X-ray and UV flares is at least 5–6 minutes. Later, at around 18:53 UT, there is a weaker UV flare on component B, which, however, is not pronounced in the total UV light curve. Because of a complicated time profile, we cannot estimate reliably the duration of the UV flare. The profile of the X-ray flare is also most likely a result of the overlapping of two flares that occurred on different components of the binary.

Finally, the time interval shown in Figure 3(d) contains another well-defined X-ray flare (F5) and its UV counterpart, both with “classical” flare profiles, peaked at around 20:42 and 20:37 UT, respectively; the UV flare occurred on component A. The UV flare was observed only partially; nevertheless, we can estimate its characteristic decay time. The X-ray flare is longer than (with $\tau_X \simeq 2\tau_{UV}$) and delayed by ~ 5 minutes with respect to the corresponding UV flare.

3.3. X-Ray Spectral Analysis

We analyzed the SXT X-ray spectra in the energy range of 0.3–7 keV using the OSPEX package (Tolbert & Schwartz 2020) and the SXT instrumental background spectrum and response files provided by the SXT team (see footnote 9).

Model X-ray spectra were fitted to the observations using the Markov Chain Monte Carlo (MCMC) approach; the MCMC sampling implementation by Anfinogentov et al. (2021) was used. Among several spectral models (see the examples and discussion in Appendix), the best agreement with the observations was achieved using the model `multi_therm_gauss` that describes optically thin bremsstrahlung radiation from multi-thermal plasma with a Gaussian dependence of the differential emission measure (DEM) on the logarithm of the temperature (T)

$$\text{DEM}(T) = \text{DEM}_0 \exp \left[-\frac{(\log T - \log T_0)^2}{2\sigma_T^2} \right], \quad (2)$$

with DEM_0 , T_0 and σ_T being the parameters of the Gaussian. The corresponding total EM and average plasma temperature ($\langle T \rangle$) are given by the formulae

$$\text{EM} = (\sqrt{2\pi} \ln 10) \text{DEM}_0 T_0 \sigma_T \exp \left(\frac{1}{2} \sigma_T^2 \ln^2 10 \right), \quad (3)$$

$$\langle T \rangle = T_0 \exp \left(\frac{3}{2} \sigma_T^2 \ln^2 10 \right). \quad (4)$$

The spectral model depended also on the abundance of heavy elements Z , relative to the solar abundance; the ratios between the elements were fixed to the solar values.

To account for the interstellar absorption, we used the model by Morrison & McCammon (1983). The absorption column density was fixed to the value of $N_H = 3 \times 10^{19} \text{ cm}^{-2}$ that was estimated using the optical extinction of $A_V = 0.017 \text{ mag}$ reported by Malkov et al. (2012) and the empirical relation of $N_H = 1.79 \times 10^{21} A_V \text{ cm}^{-2} \text{ mag}^{-1}$ by Predehl & Schmitt (1995). The effect of the interstellar absorption was found to be minor, and considering the absorption column density as a free parameter has not significantly affected the obtained results.

We performed the spectral fitting of the SXT spectra in several time intervals, including all reliably detected X-ray flares (i.e., the flares F1 and F3–F5, with the used start/end times of the flaring intervals signified by vertical dotted lines in the X-ray light curves in Figure 3) and the “quiescent” state (defined as a combination of two AstroSat orbits with the lowest X-ray flux, i.e., orbits #16303 and #16308), as well as for the entire (total) duration of the observations. An example of the SXT X-ray spectrum of AT Mic, together with the best-fit spectral model, is displayed in Figure 4 (we note that, for illustration purposes, the spectrum in Figure 4 was rebinned to reduce the number of points at high energies, while the spectral analysis was performed using the original spectral resolution). The obtained best-fit parameters of the emitting plasma are summarized in Table 2 and demonstrated in Figure 5.

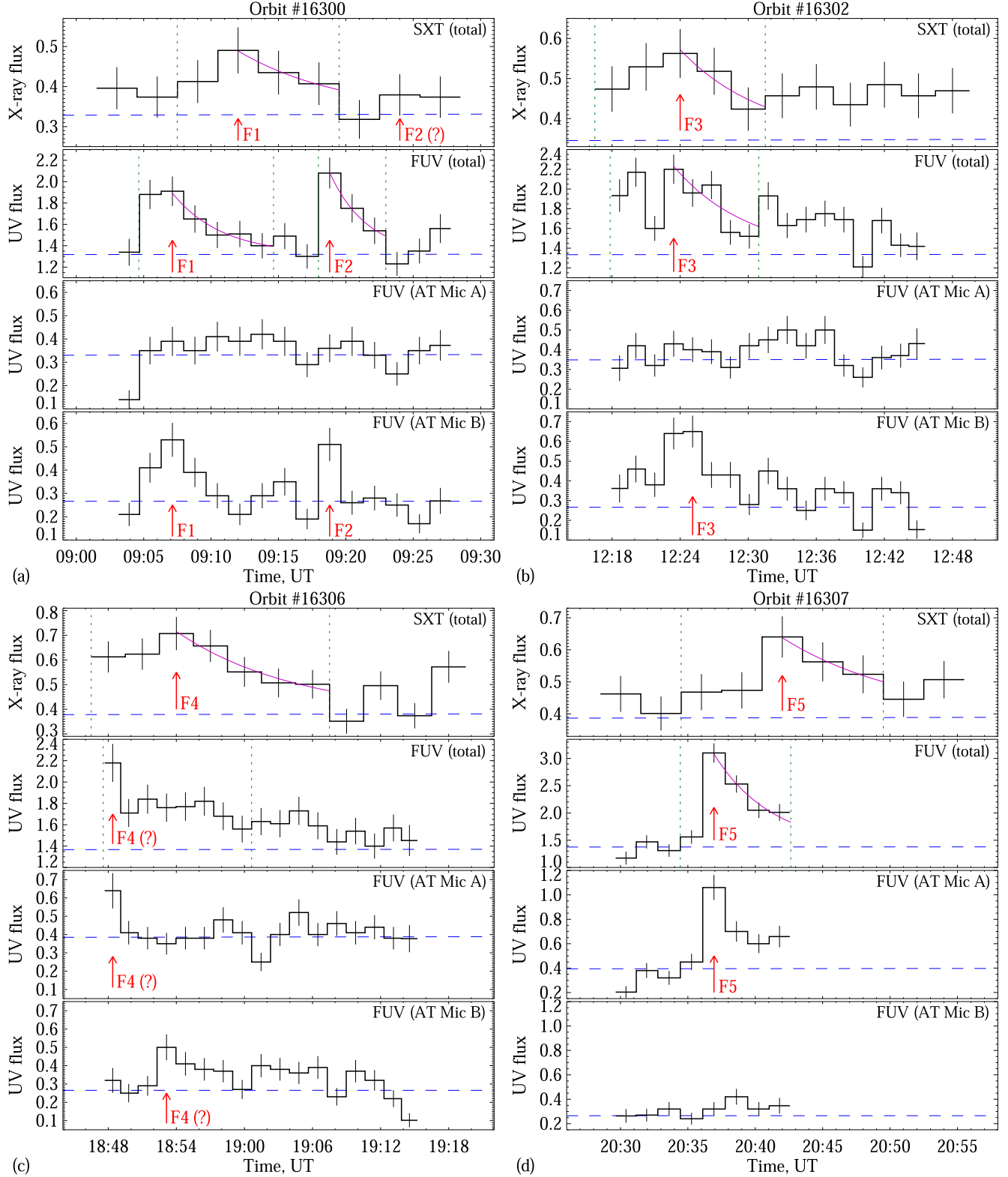


Figure 3. X-ray and UV light curves for the selected time intervals (see Figure 2) where flaring activity was detected. For the UV emission, both the total flux from the AT Mic system and the fluxes corresponding to its individual components are shown. The fluxes are in counts s^{-1} ; the time bins are 180 s and 100 s for the X-ray and UV light curves, respectively. The error bars correspond to the 1σ level. The flare IDs used in the text are written next to the red arrows. The vertical dotted lines signify the flare start/end times applied in the analysis, while the continuous magenta curves represent the exponential fits (1) to the light curves at the flare decay phases.

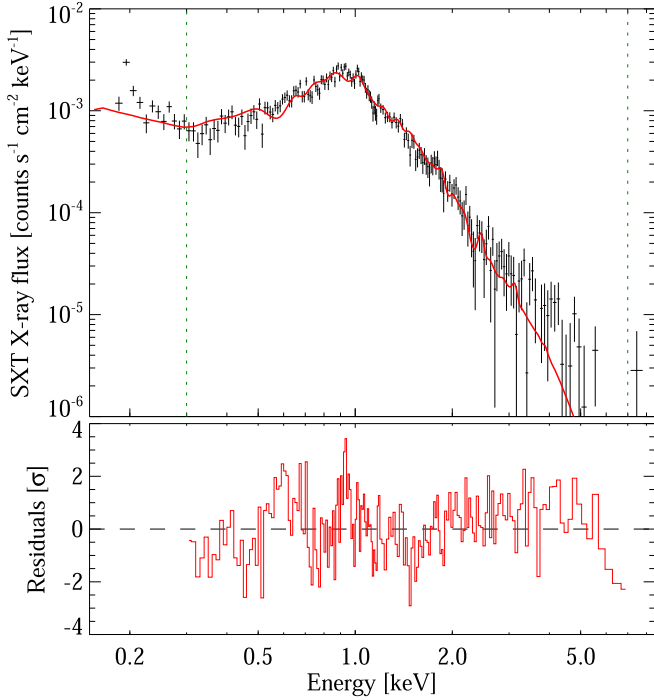


Figure 4. (Top) X-ray spectrum of AT Mic from the AstroSat SXT observations on 2018 October 3–4, averaged over the entire interval of observations. At higher energies, the original spectrum was rebinned over 2–65 channels (0.02–0.65 keV). The error bars correspond to the 1σ level. The solid red line represents a model spectral fit with the multi-thermal plasma emission model given by Equation (2). (Bottom) Normalized residuals of the model spectral fit, in units of the 1σ uncertainties.

4. Discussion

4.1. Light Curves

4.1.1. Neupert Effect

As can be seen in Figure 3 and Table 1, light curves of flares F1 and F5 (and, possibly, flare F2) demonstrate the so-called Neupert effect (Neupert 1968), when the soft X-ray flares are longer than and delayed with respect to the corresponding UV flares; the delays (~ 5 minutes) are similar in all three flares. The major UV flare F4 (on AT Mic A) was observed only partially; nevertheless, the light curves indicate a delay of at least 5–6 minutes between the X-ray and UV peaks, in agreement with the Neupert effect. In the “standard” flare model (e.g., Benz & Güdel 2010), this effect occurs because the optical or UV emissions represent a direct (and immediate) response of the chromosphere to heating by nonthermal electrons, while the soft X-rays are produced by heated plasma that evaporated from the chromosphere to the corona, with the emission intensity proportional to the cumulative (time-integrated) nonthermal energy input.

On the other hand, the flare F3 demonstrates no significant delay between the X-ray and UV peaks, and the flare durations

Table 2

Parameters of the X-ray Spectral Fits for the Selected Time Intervals: Emission Measures (EM), Average Temperatures ($\langle T \rangle$), Relative Widths of the DEM Distribution (σ_T) and Abundances of Heavy Elements (Z)

	EM, 10^{52} cm^{-3}	$\langle T \rangle$, keV	σ_T , log(keV)	Z, Z_\odot
Total	$3.54^{+0.12}_{-0.11}$	$0.728^{+0.028}_{-0.020}$	$0.168^{+0.021}_{-0.016}$	$0.192^{+0.021}_{-0.014}$
Quiescent	$2.92^{+0.29}_{-0.29}$	$0.637^{+0.053}_{-0.033}$	$0.131^{+0.050}_{-0.047}$	$0.176^{+0.070}_{-0.031}$
Flare F1	$3.33^{+0.60}_{-0.65}$	$0.680^{+0.169}_{-0.054}$	$0.117^{+0.122}_{-0.058}$	$0.185^{+0.192}_{-0.047}$
Flare F3	$3.21^{+0.45}_{-0.53}$	$1.028^{+0.464}_{-0.100}$	$0.238^{+0.100}_{-0.060}$	$0.338^{+0.282}_{-0.062}$
Flare F4	$4.42^{+0.66}_{-0.43}$	$1.199^{+1.335}_{-0.159}$	$0.384^{+0.300}_{-0.074}$	$0.273^{+0.156}_{-0.056}$
Flare F5	$3.45^{+0.61}_{-0.47}$	$0.842^{+0.417}_{-0.078}$	$0.214^{+0.167}_{-0.054}$	$0.313^{+0.205}_{-0.074}$

in both spectral ranges are similar, i.e., the Neupert effect is not pronounced. Probably, this is caused by complicated (with several separate peaks, as indicated by the UV light curve) dynamics of energy release in this flare, when the chromospheric/coronal responses to separate acts of particle acceleration are mixed together.

The Neupert effect is often (but not always) observed in solar and stellar flares (e.g., Benz & Güdel 2010). Mitra-Kraev et al. (2005), using soft X-ray and UV observations with XMM-Newton, detected the Neupert effect in flares on several red dwarfs, including AT Mic, although the reported X-ray-to-UV flare delays on AT Mic (~ 17 minutes) were longer than in our observations. Most likely, this difference is caused by the selection effect: due to a higher sensitivity and hence shorter time bins of the AstroSat UVIT (in comparison with the XMM-Newton OM), the flares detected in the UV range in this study were much shorter and weaker than those reported by Mitra-Kraev et al. (2005), and had respectively shorter delays between the X-ray and UV peaks.

4.1.2. Activity Levels of the Binary Components

In total, in the UV range (where the binary components were partially resolved) we detected four flares on component B and one or two (if we count here the partially observed flare F4) flares on component A, i.e., component B was considerably more active. A similar conclusion follows indirectly from the spatially resolved observations of AT Mic in the microwave range reported by Kundu et al. (1987): in that work, flaring activity was detected on both components of the binary, with the southern component (AT Mic B) demonstrating a stronger variability and higher microwave fluxes, although individual flares could not be identified due to short duration of the observations and insufficient time resolution. If confirmed, a higher magnetic activity of AT Mic B is most likely related to the faster rotation of this component, which results in a more efficient dynamo action (e.g., Brun & Browning 2017). On the other hand, we note that the number of detected flares in our study was too small to make a statistically significant conclusion.

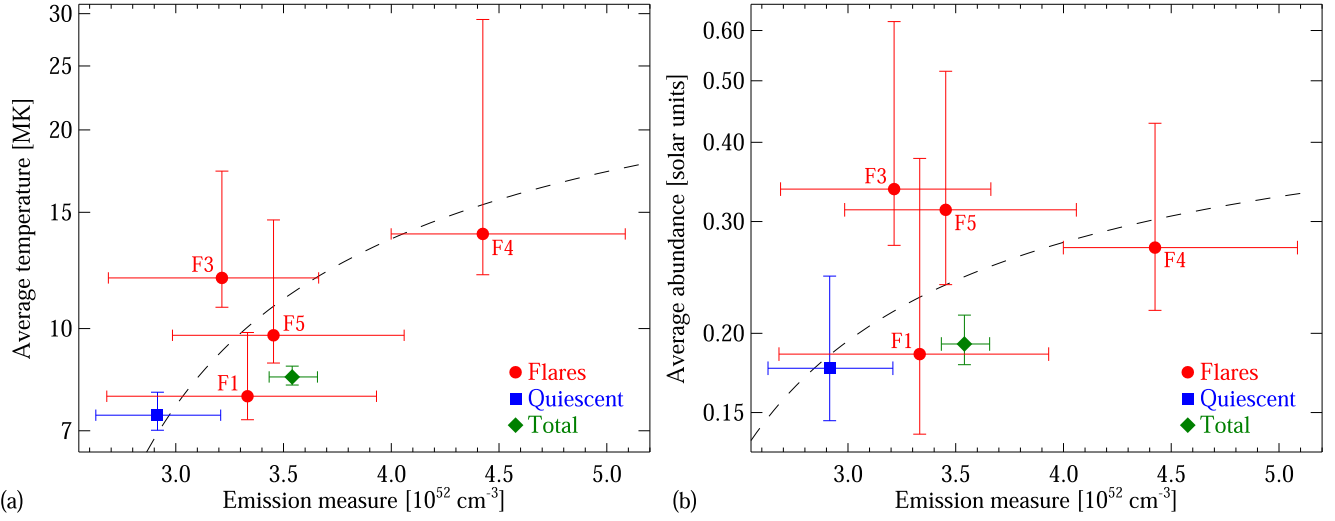


Figure 5. X-ray spectral fit parameters: average plasma temperatures (a) and abundances (b) vs. EMs in the corona of AT Mic for different time intervals. The error bars correspond to the 1σ level. The dashed lines in panels (a) and (b) represent model fits given by Equations (5) and (6), respectively.

4.2. X-Ray Spectral Fits

4.2.1. Coronal Temperatures and Emission Measures

Figure 5(a) shows the results of the X-ray spectral analysis—the EMs and average plasma temperatures for different time intervals (we note that these parameters are actually either summed or averaged over both components of the binary). In the supposedly quiescent state, the EM and average temperature are $\sim 2.9 \times 10^{52} \text{ cm}^{-3}$ and $\sim 7.4 \text{ MK}$, respectively. During flares, both the EM and average temperature increase considerably, while the time-averaged parameters for the entire duration of the observations are intermediate between the quiescent and flaring values.

Since we analyze the total emission spectra and do not separate the flaring and non-flaring spectral components, the obtained plasma temperatures during flares actually represent weighted averages of the temperatures in the quiescent coronae and in the flaring regions, which can be expressed as

$$\langle T \rangle = \frac{T_q \text{EM}_q + T_{\text{flare}}(\text{EM} - \text{EM}_q)}{\text{EM}}, \quad (5)$$

where T_q and EM_q are respectively the temperature and EM in the quiescent state, and T_{flare} is the plasma temperature in a flaring region. We have fitted Equation (5) to the observations assuming that the temperatures T_{flare} in all flaring regions are approximately the same (which is a very crude assumption) and excluding the “total” data point; the best agreement has been achieved for T_{flare} of about $31.8 \pm 20.0 \text{ MK}$. Similar temperatures ($\sim 7\text{--}8 \text{ MK}$ and $\sim 28\text{--}34 \text{ MK}$, respectively) of the quiescent and flaring plasma components in the coronae of AT Mic were reported earlier in the papers of Raassen et al. (2003)

and Robrade & Schmitt (2005), where these components were resolved spectrally.

4.2.2. Coronal Abundances

Figure 5(b) shows the EMs and coronal abundances of heavy elements for different time intervals. In the supposedly quiescent state, the coronal abundance takes its lowest value of about 0.18 of the solar photospheric abundance. The photospheric abundance for AT Mic is not exactly known; however, assuming it to be similar to that for other members of the β Pictoris association (~ 1.12 of the solar one for β Pic itself, according to Gray et al. 2006), we conclude that the corona of AT Mic is considerably depleted in heavy elements in comparison to the photosphere.

As can be seen from Figure 5(b), the coronal abundance tends to increase during flares. Most likely, this increase is caused by the chromospheric evaporation: during flares, the material from lower atmospheric layers is heated and expands upward into the coronal flaring loops, thus enriching the corona with heavy elements (we remind that in this study the measured abundances during flares actually represent weighted averages of the abundances in the quiescent coronae and in the flaring regions). The time-averaged coronal abundance (~ 0.19 of the solar photospheric abundance) is intermediate between the quiescent and flaring values, and is consistent with the coronal abundances for AT Mic reported by Robrade & Schmitt (2005). An increase of the coronal abundance during flares has been observed earlier on M dwarfs (e.g., Favata et al. 2000; Liefke et al. 2010), RS CVn binaries (e.g., Pandey & Singh 2012) and other active stars (e.g., Güdel et al. 2001).

Similarly to Equation (5), the average coronal abundance during flares (affected by the chromospheric evaporation) can

be expressed in the form

$$\langle Z \rangle = \frac{Z_q EM_q + Z_{\text{chromo}}(EM - EM_q)}{EM}, \quad (6)$$

where Z_q and Z_{chromo} are the coronal abundance in the quiescent state and the chromospheric abundance, respectively. We have fitted Equation (6) to the observations (excluding the “total” data point); the best agreement has been achieved for the chromospheric abundance Z_{chromo} of about 0.53 ± 0.32 of the solar photospheric abundance. We note that the obtained value of Z_{chromo} should be considered as an effective one, because the used model does not account for the dynamics of the chromospheric evaporation process as well as for the physical processes responsible for the underabundance of heavy elements in the corona.

4.3. Flare Energies

4.3.1. Energy Estimations

We estimate the total radiated energy of a stellar flare E^{flare} as

$$E^{\text{flare}} = \sum_i L^{\text{flare}}(t) \Delta t, \quad (7)$$

where $L^{\text{flare}}(t)$ is the time-dependent flare luminosity in the considered spectral band (see below) and Δt is the width of the time bin. The summation was performed over the time intervals bounded by vertical dotted lines in the total light curves in Figure 3. The flare luminosity in the X-ray range is given by (see Mitra-Kraev et al. 2005; Kuznetsov & Kolotkov 2021)

$$L_X^{\text{flare}}(t) = \frac{\langle L_X \rangle}{\langle I_X \rangle} [I_X(t) - I_X^{\text{bg}}(t)], \quad (8)$$

where $I_X(t)$ is the total X-ray light curve (counts s^{-1}), $I_X^{\text{bg}}(t)$ is the corresponding quiescent background X-ray flux, $\langle I_X \rangle$ is the average total X-ray flux in the selected time interval and $\langle L_X \rangle$ is the average total X-ray luminosity in the selected time interval. The latter quantity is estimated using a spectral fit

$$\langle L_X \rangle = 2\pi d^2 \int_{E_{\min}}^{E_{\max}} F(E) E \, dE, \quad (9)$$

where d is the distance to the target, $F(E)$ is the model X-ray spectral flux density and the flux in the spectral range from E_{\min} to E_{\max} is considered (0.3–7 keV in this work); this formula represents the energy flux from an optically thin source into the upper hemisphere. The peak X-ray luminosities L_X^{max} of the flares detected on AT Mic (computed using the spectral fits described in Section 3.3) are presented in Table 1.

The flare luminosity in the AstroSat FUV spectral band is given by

$$L_{\text{FUV}}^{\text{flare}}(t) = \pi d^2 G [I_{\text{FUV}}(t) - I_{\text{FUV}}^{\text{bg}}(t)], \quad (10)$$

where $I_{\text{FUV}}(t)$ is the total UV light curve (counts s^{-1}), $I_{\text{FUV}}^{\text{bg}}(t)$ is the corresponding quiescent background UV flux and G is the count rate to flux conversion factor which equals $1.545 \times 10^{-12} \text{ erg count}^{-1} \text{ cm}^{-2}$ for the UVIT FUV instrument with the F148W filter¹⁰; this formula represents the energy flux from an optically thick flat source into the upper hemisphere. While the AstroSat SXT spectral range covers most of the thermal X-ray radiation from stellar flares, the AstroSat UVIT FUV spectral band contains only a small fraction of flare radiation. Following Brasseur et al. (2019) and Fleming et al. (2022), we assume that the UV radiation of a flare can be described as blackbody radiation of hot flare ribbons, and estimate the bolometric flare luminosity $L_{\text{cont}}^{\text{flare}}$ by extrapolating the luminosity in the FUV spectral band (10) to the entire optical continuum

$$L_{\text{cont}}^{\text{flare}} = L_{\text{FUV}}^{\text{flare}} \frac{\int_0^\infty B(\lambda, T_{\text{eff}}) d\lambda}{\int_{\lambda_1}^{\lambda_2} B(\lambda, T_{\text{eff}}) d\lambda}, \quad (11)$$

where $B(\lambda, T)$ is the Planck function, T_{eff} is the effective temperature of the flare ribbons, and the wavelength range in the denominator corresponds to the bandpass of the AstroSat UVIT FUV F148W filter (125–175 nm). We use $T_{\text{eff}} = 10,000$ K as the typical effective temperature of the UV-emitting flare ribbons (Kowalski et al. 2013), with possible variations in the range of 9000–12,000 K. The extrapolation (11) is very sensitive to the adopted temperature T_{eff} , so that the uncertainty in this value is the main source of uncertainties in the estimated bolometric luminosities and radiated energies of stellar flares. The peak estimated bolometric luminosities $L_{\text{cont}}^{\text{max}}$ of the flares detected on AT Mic are presented in Table 1.

We note, however, that the bolometric luminosity estimation (11) is approximate, because, in addition to a blackbody component, the UV emission of flares can contain a significant contribution of line emission and/or Balmer continuum. As demonstrated by Kowalski et al. (2019), in the near-UV range ($\gtrsim 250$ nm) the blackbody model may underestimate the flare flux by a factor of about two; at shorter wavelengths (including the AstroSat UVIT FUV spectral band), the contribution of non-blackbody components has not been determined yet. Thus, a more accurate FUV-to-bolometric conversion would require spectroscopic observations.

The estimated radiated energies of the detected flares in the soft X-ray range and in the optical continuum are presented in Table 1. For the flare F4, only the late part was observed in the UV range; therefore, the radiated energy of this flare in the optical continuum was likely considerably (up to several times) higher than the value shown in Table 1. Also, because the decay phase of the UV flare F5 was observed only partially, the radiated energy of this flare in the optical continuum displayed in Table 1 is likely underestimated by $\sim 30\%$ (assuming an

¹⁰ <https://uvit.iap.res.in/Instrument/Filters>

exponential decay); this difference, however, is smaller than the uncertainties caused by other factors.

4.3.2. Flare Energy Partition

As follows from Table 1, the radiated energies of the detected flares were $\sim 10^{31}$ – 10^{32} erg, i.e., these flares were comparable to the strongest known solar flares (e.g., Shibata & Yokoyama 2002; Emslie et al. 2005), but far less powerful than the strongest flares observed on AT Mic before (Pallavicini et al. 1990; García-Alvarez et al. 2002). For the three flares (F1, F3 and F5), where the radiated energies both in the X-ray range and in the optical continuum are known with sufficient accuracy, we can compare the flare energy outputs in these spectral channels: the optical continuum dominated, with $E_{\text{cont}}/E_X \sim 1.4$ – 1.8 , and was responsible for $\sim 60\%$ – 65% of the total radiated flare energy. This energy partition is consistent with that in solar flares, where the white-light continuum is responsible, on average, for $\sim 70\%$ of the total radiated flare energies (Kretzschmar 2011). Similar relations between the optical and X-ray flare emissions on other stars were reported, e.g., by Guarcello et al. (2019), Schmitt et al. (2019), Kuznetsov & Kolotkov (2021).

Similarity of the flare energy partitions obtained in this and other works confirms that the above-described approach to estimate the optical continuum luminosity is justified, i.e., (a) the choice of the effective temperature of flare ribbons to be $T_{\text{eff}} = 10,000$ K is adequate, and (b) contribution of non-blackbody components in the FUV spectral band is minor.

4.4. Active Region Parameters

To estimate the parameters of the active regions on AT Mic, we use the theoretical scaling laws derived (for a magnetic reconnection model) by Maehara et al. (2015) and Namekata et al. (2017)

$$\tau \propto E^{1/3} B^{-5/3}, \quad \tau \propto E^{-1/2} L^{5/2}, \quad (12)$$

where τ is the flare duration, E is the released flare energy, B is the characteristic magnetic field strength in the flaring region and L is the length scale of the flaring region; the scaling coefficients were determined from observations of solar flares. For consistency with the results of Namekata et al. (2017), we characterize a flare with the radiated energy in the optical continuum (assuming $E \simeq E_{\text{cont}}$) and the optical/UV decay timescale (assuming $\tau \simeq \tau_{\text{UV}}$); therefore we consider four flares (F1–F3 and F5) where these parameters were reliably determined. The estimated parameters of the corresponding flaring regions are presented in Table 1. The flaring regions on AT Mic had typical sizes of about 35,000–70,000 km and typical magnetic field strengths of about 80–120 G (we note that the used scaling laws provide an average magnetic field strength in the flaring volume in the solar/stellar corona, while the field strength at the photospheric level can be much higher).

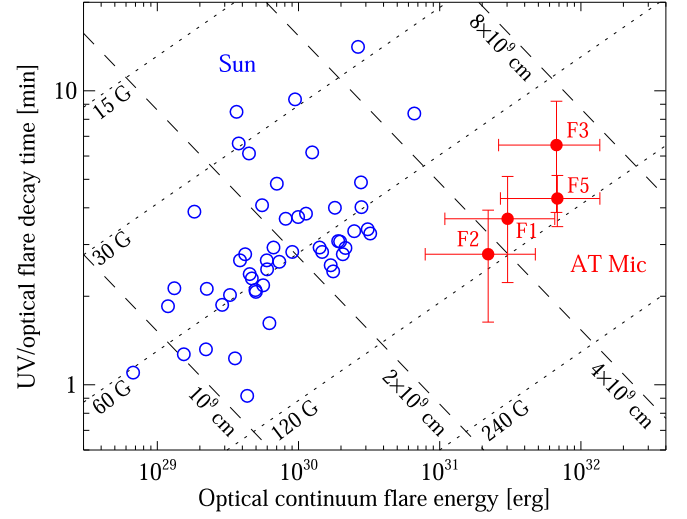


Figure 6. UV/optical flare decay times vs. the optical continuum flare energies for the flares on the Sun (from Namekata et al. 2017, marked by empty blue circles) and AT Mic (obtained in this work, signified by filled red circles). The dashed and dotted lines represent the theoretical scaling laws by Namekata et al. (2017). The error bars (shown for the stellar flares only) correspond to the 1σ level.

In Figure 6, we compare the radiated energies and decay times of the flares detected on AT Mic in this study with the respective parameters of the solar flares (of the GOES classes M1.0–X2.8) reported by Namekata et al. (2017); we also overplot theoretical isolines of characteristic magnetic field strength or flaring region size predicted by the scaling laws (12) (see similar plots for flares on other stars in the papers of Namekata et al. 2017, 2018; Brasseur et al. 2019; Tu et al. 2020; Ramsay et al. 2021; Tu et al. 2021, etc.). The flaring region sizes on AT Mic seem to be comparable to or slightly larger than those for the largest solar flares. On the other hand, the magnetic field strengths in the flaring regions on AT Mic are considerably (by a factor of ~ 1.5 – 2) higher than the typical values in the solar flaring regions. A similar conclusion (i.e., that the magnetic fields in stellar flaring regions are typically stronger than in solar ones) was made earlier by Namekata et al. (2017, 2018) for the stellar flares observed with Kepler in the short cadence (1 minute) mode and by Tu et al. (2020, 2021) for the stellar flares observed with TESS.

The question is open whether the above mentioned differences between the solar and stellar flares are qualitative or quantitative, i.e., whether flares similar to the flares described here on AT Mic can occur on the Sun, albeit rarely. A possible close solar analog of the stellar events was the X9.3 class solar flare on 2017 September 6 that, despite its high energetics ($\sim 10^{31}$ erg), was relatively short and compact; notably, an anomalously strong magnetic field (up to ~ 4000 G in the low corona) was detected in that flare (Anfinogentov et al. 2019). Such rare solar flares with extremely strong

magnetic fields deserve further study, because they may bridge the gap between “ordinary” solar flares and stellar superflares.

5. Summary and Conclusions

We observed the active M-dwarf binary AT Mic with the orbital observatory AstroSat. The target was detected by the SXT telescope in the soft X-ray range (0.3–7 keV) and by the UVIT telescope in the far-UV range (130–180 nm), with ~ 10 ks of simultaneous observations in the two spectral ranges. The main results can be summarized as follows:

1. In both the X-ray and UV spectral ranges, we detected quiescent emission and a number of flares. Using the spatially resolved UV observations, we have for the first time identified reliably the components of the binary where the flares occurred: two flares on AT Mic A and four flares on AT Mic B.
2. The X-ray flares were typically longer than (by a factor of ~ 2) and delayed after (by ~ 5 – 6 minutes) their UV counterparts, demonstrating the Neupert effect.
3. The X-ray-emitting coronal plasma has been found to be best described by a multi-temperature distribution. In the quiescent state, the EM was $\sim 2.9 \times 10^{52} \text{ cm}^{-3}$ and the average temperature was ~ 7 MK. During flares, both the EM and average temperature increased (up to $\sim 4.5 \times 10^{52} \text{ cm}^{-3}$ and ~ 15 MK, respectively), corresponding to the plasma temperature in the flaring regions of ~ 32 MK.
4. The abundance of heavy elements in the corona of AT Mic has been found to be much lower than at the Sun ($\sim 0.18 Z_{\odot}$ in the quiescent state). During flares, the coronal abundance increased (up to $\sim 0.34 Z_{\odot}$), due to chromospheric evaporation.
5. The detected flares had the radiated energies of $\sim 10^{31}$ – 10^{32} erg. The optical continuum emission dominated and was responsible for $\sim 60\%$ – 65% of the total radiated flare energy.
6. The estimated sizes of flaring regions on AT Mic ($\sim 35,000$ – $70,000$ km) are comparable to or slightly larger than those for the largest solar flares. On the other hand, the estimated magnetic field strengths in the flaring regions on AT Mic (~ 80 – 120 G) are ~ 1.5 – 2 times higher than those in typical solar flares.

Acknowledgments

This work was supported by the BRICS Multilateral Research and Development Projects-2016 (DST/MRCK/BRICS/PilotCall1/Superflares/2017), the project “Superflares on stars and the Sun,” the Russian Foundation for Basic Research under Grant 17-52-80064, and the Ministry of Science and Higher Education of the Russian Federation. K.C. is supported by the Research Council of Norway through its Centres of Excellence scheme (project No. 262622). This

research is based on the results obtained from the AstroSat mission of the Indian Space Research Organisation (ISRO), archived at the Indian Space Science Data Centre (ISSDC). This work has used the UVIT data processed by the payload operations center at IIA; the UVIT was built in collaboration between IIA, IUCAA, TIFR, ISRO and CSA. This work has used the data from the SXT developed at TIFR, Mumbai, and the SXT POC at TIFR is thanked for verifying and releasing the data via the ISSDC data archive and providing the necessary software tools.

Appendix Comparison of Different X-Ray Spectral Models

In order to estimate the parameters of the emitting plasma, we performed fitting of the observed soft X-ray spectra of AT Mic with several spectral models using the MCMC approach; the MCMC sampling implementation by Anfinogentov et al. (2021) was used. In this section, we present the results obtained for the SXT spectrum averaged over the entire (total) duration of the observations, and for the time interval corresponding to the flare F4 that was the strongest X-ray flare in our observations; the analysis of other time intervals provided qualitatively similar results. We have considered three plasma emission models: (a) the single-temperature optically thin thermal model (vth) depending on the EM, temperature T and metallicity Z ; (b) the double-temperature optically thin thermal model (2vth) depending on the EMs EM_1 and EM_2 of two plasma components, the temperatures T_1 and T_2 of the respective plasma components and metallicity Z ; (c) the multi-temperature optically thin thermal model with a Gaussian dependence of the DEM on the logarithm of the temperature as described by Equations (2)–(4) (multi_therm_gauss), depending on the total EM, the average plasma temperature $\langle T \rangle$, the width of the DEM distribution σ_T and metallicity Z . Figures A1–A3 demonstrate the results of the MCMC analysis: the posterior probability distributions for the above mentioned spectral models and time intervals; the best-fit model parameters (i.e., the most probable values of the parameters that also correspond to the minimum values of the χ^2 statistics) are shown as well. Figure A4 compares the spectral fits obtained using different spectral models.

One can see in Figure A4 that, in comparison with the single-temperature model, the double-temperature model provides better fits to the observations at high energies ($\gtrsim 2$ keV) and also noticeably lower overall χ^2 values. The secondary plasma component (i.e., the component with the higher temperature) comprises a significant part of the emitting plasma, with the EM_2/EM_1 ratio varying from 0.12 for the total duration of the observations up to 0.27 during the flares. These results indicate the presence of at least two plasma components with different temperatures. On the other hand, the temperature of the secondary component T_2 in the double-temperature model remains unconstrained, when the values in a very broad range have comparable

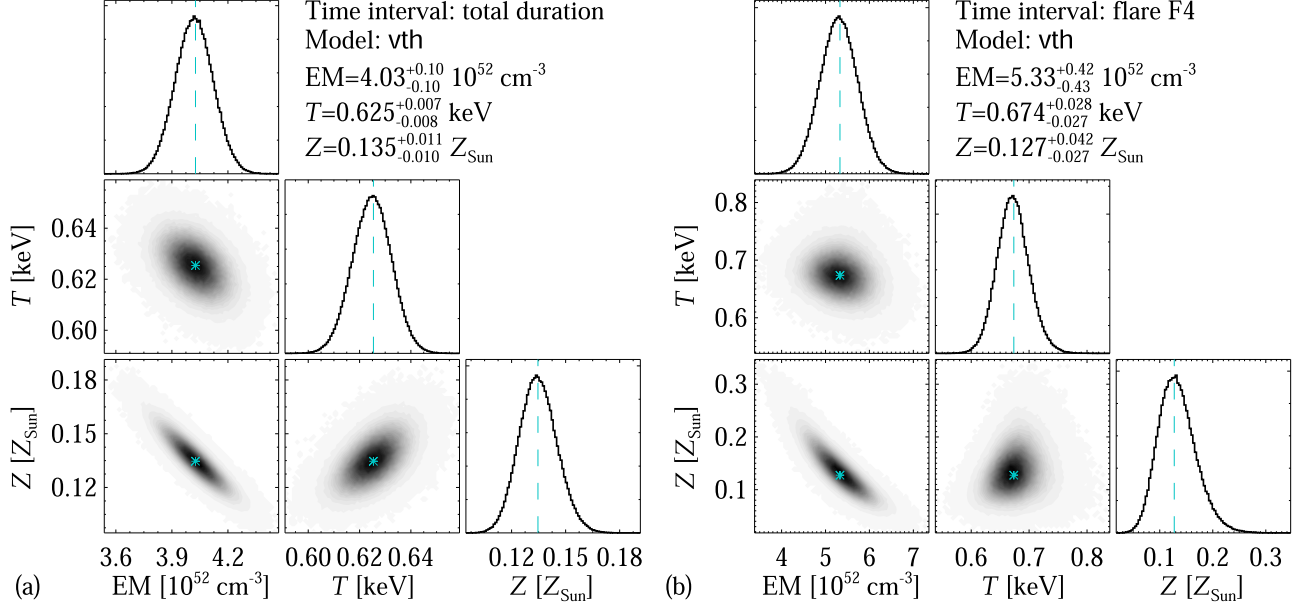
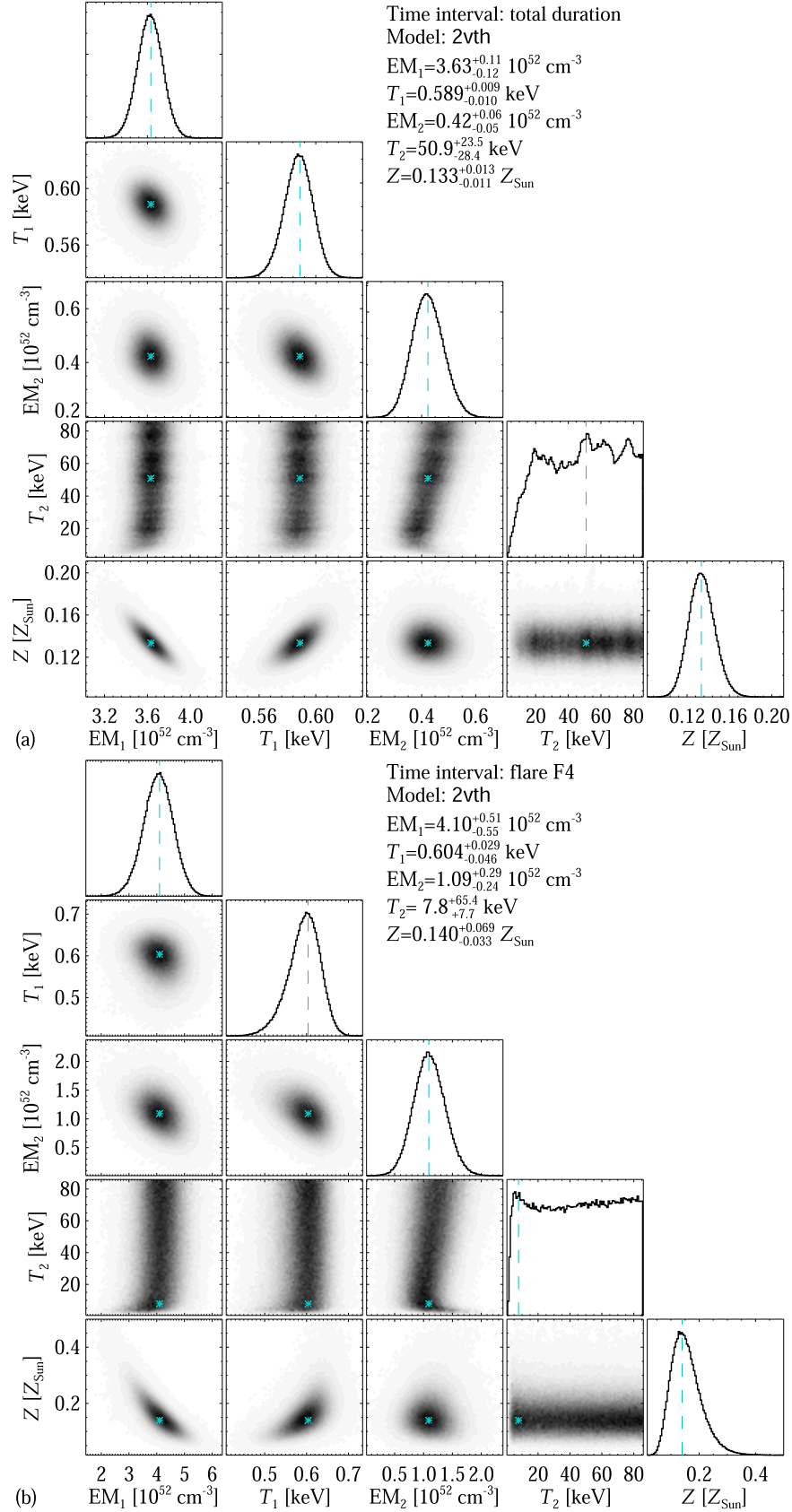


Figure A1. Results of the MCMC analysis of the AstroSat SXT X-ray spectra of AT Mic using the single-temperature optically thin thermal model (vth). The posterior probability distributions are depicted, with gray-scale 2D plots depicting the joint posterior probability distributions for different combinations of the model parameters (darker areas correspond to higher probability), and histograms demonstrating the marginal posterior probability distributions of the individual parameters. Two time intervals are considered: (a) the total duration of the observations, and (b) flare F4. The most probable values of the model parameters with the 1σ (68%) confidence intervals are displayed in the panels as well.

**Figure A2.** Same as in Figure A1, for the double-temperature optically thin thermal model (2vth).

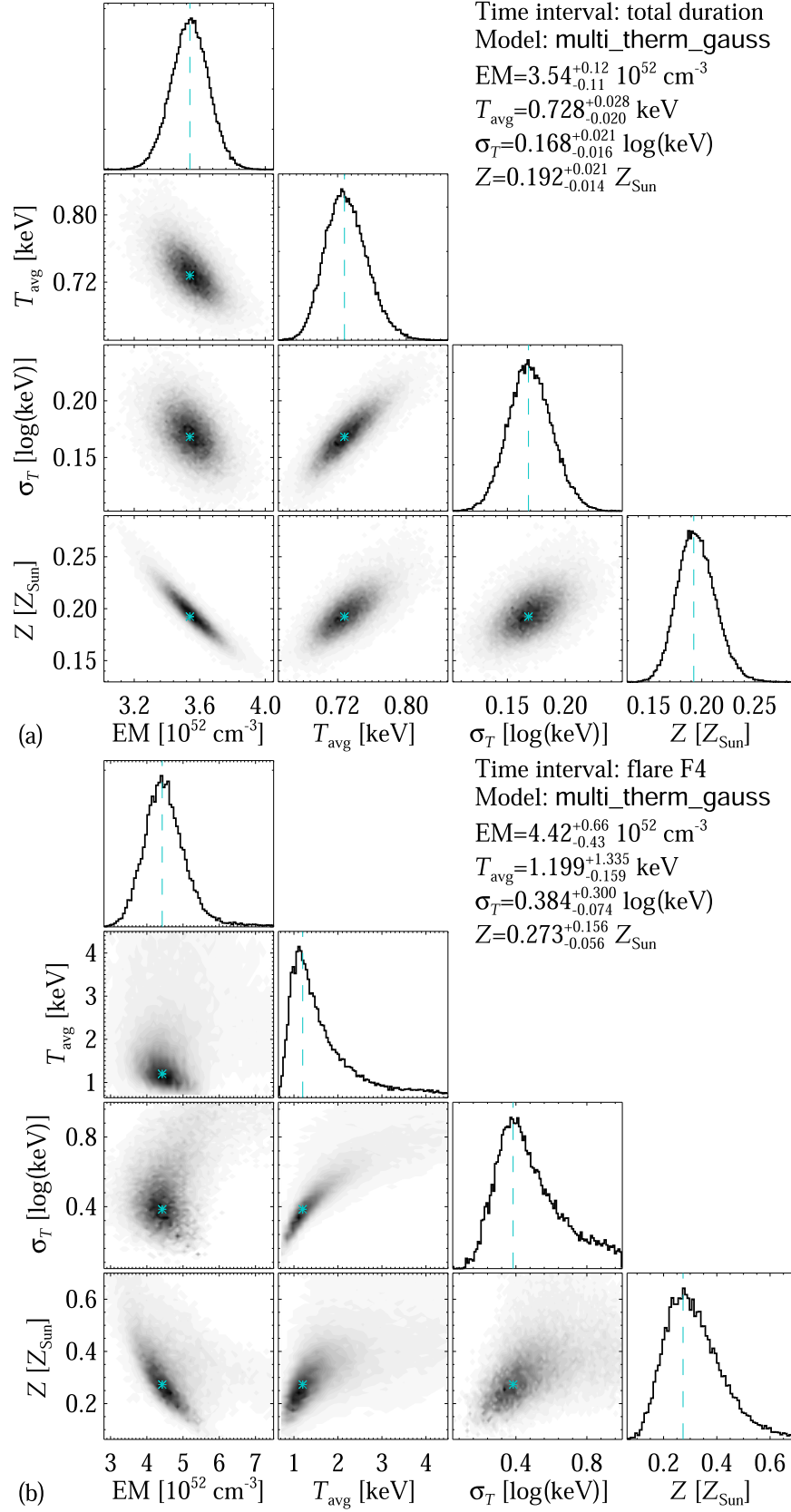


Figure A3. Same as in Figures A1–A2, for the optically thin thermal model with a Gaussian DEM distribution (multi_therm_gauss).

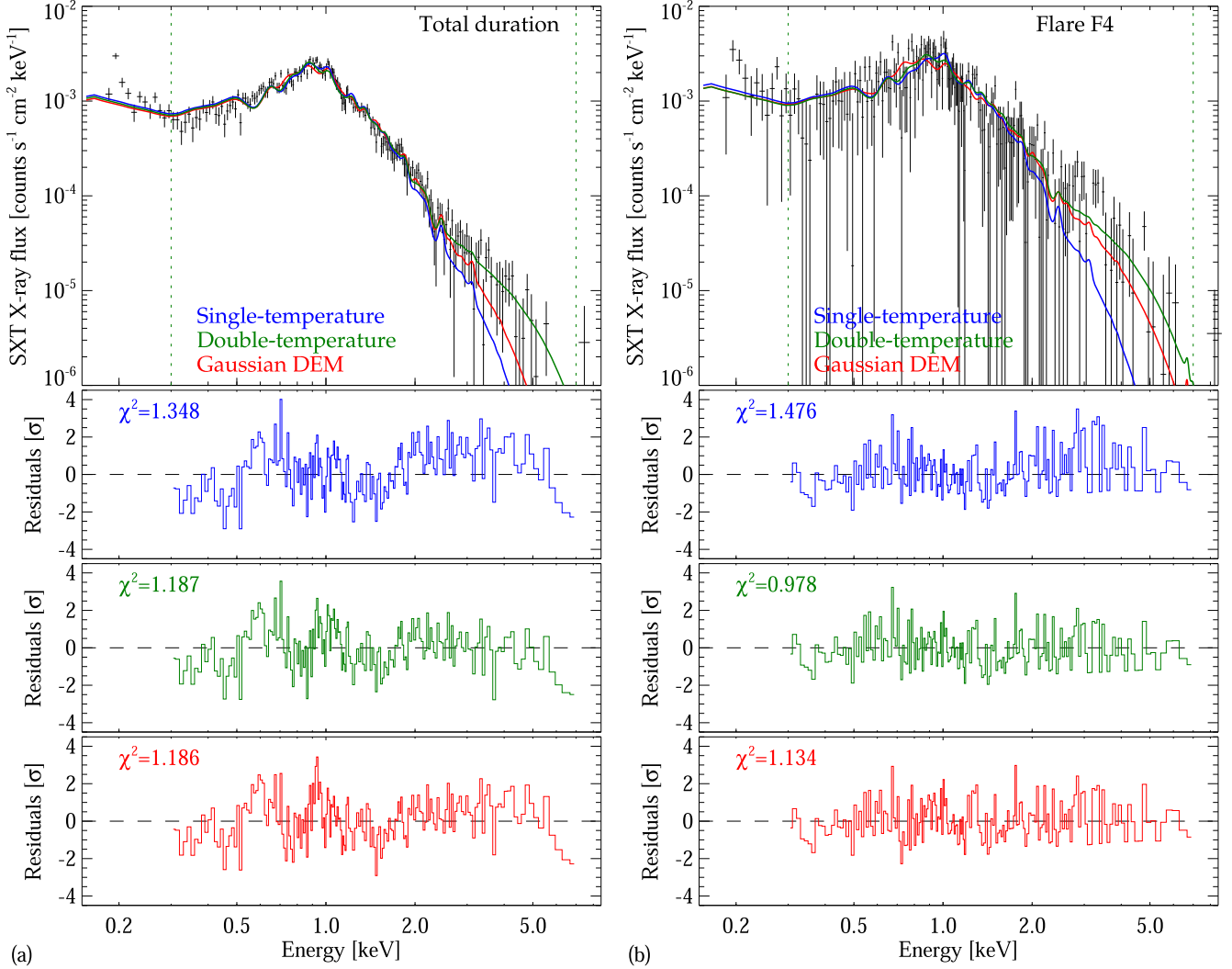


Figure A4. (Top) X-ray spectra of AT Mic obtained with the AstroSat SXT on 2018 October 3–4, for the entire interval of observations (a) and for the flare F4 (b). At higher energies, the original spectra are rebinned over 2–65 channels (0.02–0.65 keV). The error bars correspond to the 1σ level. The solid lines represent the best spectral fits with three different plasma emission models obtained using the MCMC technique (see Figures A1–A3 for the best-fit model parameters). (Bottom) Normalized residuals of the model spectral fits for the considered plasma emission models, in units of the 1σ uncertainties; the respective values of the χ^2 statistic are shown as well.

posterior probabilities (see Figure A2) and provide equally good spectral fits; therefore the double-temperature model, while providing useful insights, cannot be used for a reliable quantitative analysis. The uncertainty in determining the secondary component temperature can indicate that this secondary component itself has a complicated composition which cannot be described by a single temperature.




The multi-temperature model with a Gaussian DEM distribution is intermediate (in terms of the number of parameters) between the single-temperature and double-temperature models. It is reduced to a single-temperature model when the width parameter σ_T approaches zero, while it can account for contributions of multiple plasma components with temperatures in a broad range around the

peak temperature for larger values of σ_T . We have found that the parameters of this model are well constrained by the observations (see Figure A3), while the quality of spectral fits (in terms of χ^2) is noticeably better than that for the single-temperature model and comparable to (or only slightly worse than) that for the double-temperature model (see Figure A4). Therefore we conclude that, among the considered models, the multi-temperature spectral model `multi_therm_gauss` is the most suitable one to analyze the AstroSat SXT observations of AT Mic.

The presence of multi-thermal plasma in the coronae of red dwarfs, including AT Mic, has been reported in earlier studies as well, e.g., Robrade & Schmitt (2005), using the XMM-Newton observations, obtained for AT Mic the DEM

distribution with a peak at $T_0 = 7$ MK and FWHM of about 6 MK, which corresponds to $\sigma_T \simeq 0.15$ in Equation (2); these estimations are consistent with our results for the total duration of the observations (see Table 2).

ORCID iDs

A. A. Kuznetsov  <https://orcid.org/0000-0001-8644-8372>
 K. Chandrashekhara  <https://orcid.org/0000-0001-5803-0649>
 D. Banerjee  <https://orcid.org/0000-0003-4653-6823>

References

- Agrawal, P. C. 2017, *JApA*, **38**, 27
 Agrawal, P. C., Yadav, J. S., Antia, H. M., et al. 2017, *JApA*, **38**, 30
 Anfinogentov, S. A., Nakariakov, V. M., Pascoe, D. J., & Goddard, C. R. 2021, *ApJS*, **252**, 11
 Anfinogentov, S. A., Stupishin, A. G., Mysh'akov, I. I., & Fleishman, G. D. 2019, *ApJL*, **880**, L29
 Benz, A. O., & Güdel, M. 2010, *ARA&A*, **48**, 241
 Bhalerao, V., Bhattacharya, D., Vibhute, A., et al. 2017, *JApA*, **38**, 31
 Brasseur, C. E., Osten, R. A., & Fleming, S. W. 2019, *ApJ*, **883**, 88
 Brun, A. S., & Browning, M. K. 2017, *LRSP*, **14**, 4
 Elgaroy, O., Joras, P., Engvold, O., et al. 1988, *A&A*, **193**, 211
 Emslie, A. G., Dennis, B. R., Holman, G. D., & Hudson, H. S. 2005, *JGRA*, **110**, A11103
 Favata, F., Reale, F., Micela, G., et al. 2000, *A&A*, **353**, 987
 Fleming, S. W., Million, C., Osten, R. A., Kolotkov, D. Y., & Brasseur, C. E. 2022, *ApJ*, **928**, 8
 Gaia Collaboration 2020, *yCat*, **1350**, 0
 García-Alvarez, D., Jevremović, D., Doyle, J. G., & Butler, C. J. 2002, *A&A*, **383**, 548
 Gershberg, R. E. 2005, *Solar-Type Activity in Main-Sequence Stars* (Berlin: Springer)
 Gershberg, R. E., Katsova, M. M., Lovkaya, M. N., Terebizh, A. V., & Shakhovskaya, N. I. 1999, *A&AS*, **139**, 555
 Gray, R. O., Corbally, C. J., Garrison, R. F., et al. 2006, *AJ*, **132**, 161
 Guarcello, M. G., Micela, G., Sciortino, S., et al. 2019, *A&A*, **622**, A210
 Güdel, M. 2002, *ARA&A*, **40**, 217
 Güdel, M. 2004, *A&ARv*, **12**, 71
 Güdel, M., Audard, M., Briggs, K., et al. 2001, *A&A*, **365**, L336
 Haisch, B., Strong, K. T., & Rodono, M. 1991, *ARA&A*, **29**, 275
 Joy, A. H., & Abt, H. A. 1974, *ApJS*, **28**, 1
 Kowalski, A. F., Hawley, S. L., Wisniewski, J. P., et al. 2013, *ApJS*, **207**, 15
 Kowalski, A. F., Wisniewski, J. P., Hawley, S. L., et al. 2019, *ApJ*, **871**, 167
 Kretzschmar, M. 2011, *A&A*, **530**, A84
 Kundu, M. R., Jackson, P. D., White, S. M., & Melozzi, M. 1987, *ApJ*, **312**, 822
 Kunkel, W. E. 1970, *Inf. Bull. Var. Stars*, **442**, 1
 Kuznetsov, A. A., & Kolotkov, D. Y. 2021, *ApJ*, **912**, 81
 Liefke, C., Fuhrmeister, B., & Schmitt, J. H. M. M. 2010, *A&A*, **514**, A94
 Linsky, J. L., Bornmann, P. L., Carpenter, K. G., et al. 1982, *ApJ*, **260**, 670
 Maehara, H., Shibayama, T., Notsu, Y., et al. 2015, *EP&S*, **67**, 59
 Malkov, O. Y., Tamazian, V. S., Docobo, J. A., & Chulkov, D. A. 2012, *A&A*, **546**, A69
 Mason, K. O., Breeveld, A., Much, R., et al. 2001, *A&A*, **365**, L36
 Messina, S., Leto, G., & Pagano, I. 2016, *A&SS*, **361**, 291
 Messina, S., Millward, M., Buccino, A., et al. 2017, *A&A*, **600**, A83
 Mitra-Kraev, U., Harra, L. K., Güdel, M., et al. 2005, *A&A*, **431**, 679
 Monsignori, F. B. C., Landini, M., Drake, J. J., & Cully, S. L. 1995, *A&A*, **302**, 193
 Morrison, R., & McCammon, D. 1983, *ApJ*, **270**, 119
 Namekata, K., Sakaue, T., Watanabe, K., et al. 2017, *ApJ*, **851**, 91
 Namekata, K., Sakaue, T., Watanabe, K., et al. 2018, *IAUS*, **340**, 221
 Nelson, G. J., Robinson, R. D., Slee, O. B., et al. 1986, *MNRAS*, **220**, 91
 Neupert, W. M. 1968, *ApJL*, **153**, L59
 Pallavicini, R., Tagliaferri, G., & Stella, L. 1990, *A&A*, **228**, 403
 Pandey, J. C., & Singh, K. P. 2012, *MNRAS*, **419**, 1219
 Perdelwitz, V., Czesla, S., Robrade, J., Pribulla, T., & Schmitt, J. H. M. M. 2018, *A&A*, **619**, A138
 Predehl, P., & Schmitt, J. H. M. M. 1995, *A&A*, **500**, 459
 Raassen, A. J. J., Mewe, R., Audard, M., & Güdel, M. 2003, *A&A*, **411**, 509
 Ramsay, G., Kolotkov, D., Doyle, J. G., & Doyle, L. 2021, *SoPh*, **296**, 162
 Reiners, A. 2012, *LRSP*, **9**, 1
 Robrade, J., & Schmitt, J. H. M. M. 2005, *A&A*, **435**, 1073
 Schmitt, J. H. M. M., Ioannidis, P., Robrade, J., Czesla, S., & Schneider, P. C. 2019, *A&A*, **628**, A79
 Shibata, K., & Yokoyama, T. 2002, *ApJ*, **577**, 422
 Singh, K. P., Tandon, S. N., Agrawal, P. C., et al. 2014, *Proc. SPIE*, **9144**, 91441S
 Singh, K. P., Stewart, G. C., Chandra, S., et al. 2016, *Proc. SPIE*, **9905**, 99051E
 Singh, K. P., Stewart, G. C., Westergaard, N. J., et al. 2017, *JApA*, **38**, 29
 Strüder, L., Briel, U., Dennerl, K., et al. 2001, *A&A*, **365**, L18
 Tandon, S. N., Subramaniam, A., Girish, V., et al. 2017a, *AJ*, **154**, 128
 Tandon, S. N., Hutchings, J. B., Ghosh, S. K., et al. 2017b, *JApA*, **38**, 28
 Tolbert, K., & Schwartz, R. 2020, OSPEX: Object Spectral Executive, Astrophysics Source Code Library, ascl:2007.018
 Tsang, B. T. H., Pun, C. S. J., Di Stefano, R., Li, K. L., & Kong, A. K. H. 2012, *ApJ*, **754**, 107
 Tu, Z.-L., Yang, M., Wang, H. F., & Wang, F. Y. 2021, *ApJS*, **253**, 35
 Tu, Z.-L., Yang, M., Zhang, Z. J., & Wang, F. Y. 2020, *ApJ*, **890**, 46
 Turner, M. J. L., Abbey, A., Arnaud, M., et al. 2001, *A&A*, **365**, L27
 Yadav, J. S., Agrawal, P. C., Antia, H. M., et al. 2016, *Proc. SPIE*, **9905**, 99051D